



# A detailed comparison of single-camera light-field PIV and tomographic PIV

Shengxian Shi<sup>1</sup> · Junfei Ding<sup>1</sup> · Callum Atkinson<sup>2</sup> · Julio Soria<sup>2,3</sup> · T. H. New<sup>4</sup>

Received: 6 July 2017 / Revised: 12 December 2017 / Accepted: 22 January 2018 / Published online: 10 February 2018  
© Springer-Verlag GmbH Germany, part of Springer Nature 2018

## Abstract

This paper conducts a comprehensive study between the single-camera light-field particle image velocimetry (LF-PIV) and the multi-camera tomographic particle image velocimetry (Tomo-PIV). Simulation studies were first performed using synthetic light-field and tomographic particle images, which extensively examine the difference between these two techniques by varying key parameters such as pixel to microlens ratio (PMR), light-field camera Tomo-camera pixel ratio (LTPR), particle seeding density and tomographic camera number. Simulation results indicate that the single LF-PIV can achieve accuracy consistent with that of multi-camera Tomo-PIV, but requires the use of overall greater number of pixels. Experimental studies were then conducted by simultaneously measuring low-speed jet flow with single-camera LF-PIV and four-camera Tomo-PIV systems. Experiments confirm that given a sufficiently high pixel resolution, a single-camera LF-PIV system can indeed deliver volumetric velocity field measurements for an equivalent field of view with a spatial resolution commensurate with those of multi-camera Tomo-PIV system, enabling accurate 3D measurements in applications where optical access is limited.

## 1 Introduction

Volumetric 3-component 3-dimensional (3C-3D) velocity measurements have long been a goal of the experimental fluid mechanics community, as it provides an important means to reveal the physics of complex flows. Through more than three decades of evolution, particle image velocimetry (PIV) has progressed from 2-component 2-dimensional (2C-2D) and 3-component 2-dimensional (3C-2D) measurements to full 3C-3D flow diagnostics (Adrian 1984; Adrian and Westerweel 2011). One of the most highly performing and widely applied volumetric PIV techniques is the

tomographic PIV (Tomo-PIV, Elsinga et al. 2006; Scarano 2013), which possesses many attractive features when compared to other 3C-3D PIV techniques. For instance, it can handle much higher seeding density and subsequently achieve higher spatial resolution than Defocusing Digital PIV (DDPIV, Pereira et al. 2000) and digital Holographic PIV (HPIV, Hinsch 2002; Meng et al. 2004), particularly when combined with time-resolved Lagrangian particle tracking (Schanz et al. 2016), and requires relatively less cameras (typically 4–8 cameras) when compared to the Synthetic Aperture PIV (SAPIV, Belden et al. 2010), which needs 8–15 cameras to cover an equivalent measurement volume.

A significant limitation of Tomo-PIV is that it requires the use of multiple views and cameras, the arrangement of which necessitates the use of a large experimental space and multiple paths of optical accesses to the measurement area. This may be problematic for many space-constrained applications and internal industrial flows where it may not be possible to have multiple optical windows or to perform in situ camera calibration. For instance, applications such as blade tip leakage and secondary passage flow in gas turbines, which are the key sources of the reduced efficiency of turbines and compressors and can significantly impact on blade life. Driven by the significant pressure difference across these blades, such flows are highly three dimensional

✉ Shengxian Shi  
kirinshi@sjtu.edu.cn

<sup>1</sup> School of Mechanical Engineering, Shanghai Jiao Tong University, Shanghai 200240, China

<sup>2</sup> Laboratory for Turbulence Research in Aerospace and Combustion, Department of Mechanical and Aerospace Engineering, Monash University, Melbourne, VIC 3800, Australia

<sup>3</sup> Department of Aeronautics, King Abdulaziz University, Jeddah, Kingdom of Saudi Arabia

<sup>4</sup> School of Mechanical and Aerospace Engineering, Nanyang Technological University, 50 Nanyang Avenue, Singapore 639798, Singapore

and quantitative measurements are further complicated by the small clearances between the blade tips and casings (e.g. typically 1–2% of blade span). Accurate characterisation of such flows has long been a challenge for experimental research in gas turbines and only very limited 2C-2D or 3C-2D flow measurements have been successfully performed (Wernet et al. 2005; Palafox et al. 2008). As such, single-camera-based volumetric flow diagnostic techniques with large measurable volume and high spatial resolution are highly desirable for these space-constrained applications.

One such technique is the single-camera-based light-field particle image velocimetry (abbreviated as LF-PIV hereafter) (Ding et al. 2015; Fahringer et al. 2015; Shi et al. 2016, 2017; Xu et al. 2017; Li et al. 2017). As the name implies, LF-PIV relies on light-field photography to capture 3D information of tracer particles. Unlike SAPIV which employs a camera array to record the light-field of particle images, LF-PIV achieves similar functionality using a light-field camera, which combines a high-resolution microlens array (MLA) with a CCD/CMOS sensor. Although LF-PIV has been successfully applied to cylinder wake and jet flow measurements, a comprehensive comparison between the performance of LF-PIV and the more widely used Tomo-PIV has not been reported. In particular, it will be instructive to observe how measurement uncertainty will differ between LF-PIV and Tomo-PIV when the number of cameras used by Tomo-PIV varies. Furthermore, with the ever-increasing pixel resolution of digital image sensor technology, it will be worthwhile to predict the LTPR at which LF-PIV is able to achieve equivalent accuracy in the  $x$ -,  $y$ - and  $z$ -direction than Tomo-PIV.

To address these questions, the present study uses a series of synthetic light-field and tomographic particle images to investigate the effects of Tomo-PIV camera number and the pixel resolution ratio between light-field and Tomo-PIV cameras on the accuracy of the reconstructed particle distributions and associated velocity. In addition, a direct experimental comparison between LF-PIV and Tomo-PIV was conducted on a jet facility to better quantify the practical challenges and differences between these two techniques. In the following sections, information on the synthetic image generation and detailed simulation studies will be provided, followed by detailed descriptions on the experimental setup and the flow reconstruction results.

## 2 Numerical analysis with synthetic particle images

Before delving into a detailed comparison of LF-PIV and Tomo-PIV, it is important to identify the key factors that affect the measurement accuracy of these two techniques. In the case of Tomo-PIV, it is known that the performance is

strongly affected by the number of cameras and the seeding density (Elsinga et al. 2006; Atkinson and Soria 2009). For LF-PIV, the identification of key performance parameters is not as straightforward. In light-field camera (Ng et al. 2005), the MLA is positioned one focal length away from the CCD/CMOS sensor, which ensures the highest available angular resolution (Fig. 1a). In focused light-field camera (Fig. 1b), the distance between the MLA and CCD/CMOS sensor is variable and different levels of spatial resolution (resolution in each refocused slice) can be achieved by sacrificing angular resolution (Georgiev et al. 2006; Lumsdaine and Georgiev 2009).

For volumetric velocity measurements, higher angular resolution is preferred over the in-plane spatial resolution as it leads to a greater information about particle displacement in the direction normal to the imaging plane. Hence, current LF-PIV techniques all made use of light-field cameras (Ding et al. 2015; Fahringer et al. 2015; Shi et al. 2017). Previous studies indicate that the performance of LF-PIV is mostly affected by the pixel–microlens ratio (PMR) as angular resolution is determined by number of pixels beneath each lenslet. In addition, higher MLA resolution can tolerate higher seeding density (Shi et al. 2016). As such, it is preferable for LF-PIV to achieve as high a pixel resolution as possible, so as to produce high angular resolution (large PMR) as well as high spatial resolution (high MLA resolution). Therefore, PMR is the key factor that affects the performance of LF-PIV. When comparing LF-PIV and Tomo-PIV, it is important to consider the number of pixels required in LF-PIV

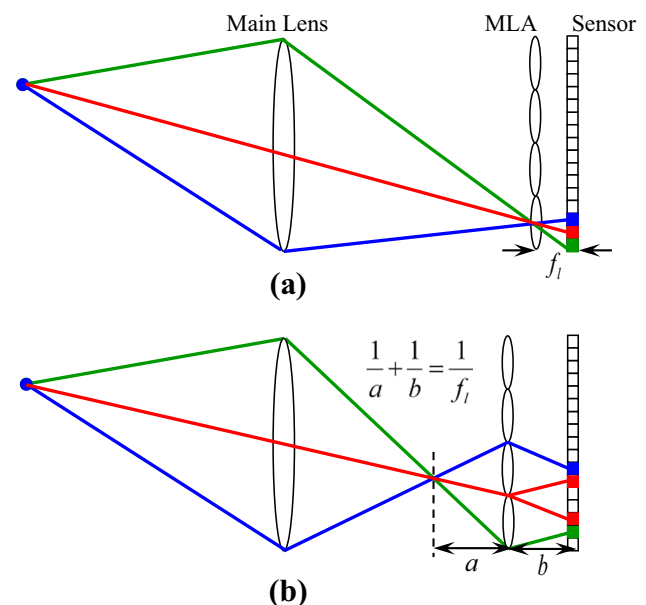


**Fig. 1** Schematics of light-field imaging techniques based on **a** light-field camera and **b** focused light-field camera (colour only in electronic version)

compared to the total number of pixels that are employed in a multi-camera Tomo-PIV experiment. To characterise this, we defined a pixel ratio between light-field and Tomo-system [Light-field camera Tomo-cameras pixel ratio,  $LTPR = \frac{(p_x \times p_y)_{LF-PIV}}{(p_x \times p_y \times N_c)_{Tomo-PIV}}$ ,] which if we consider camera cost in terms of dollars per pixels can be taken as representative of the comparative cost of these two experimental approaches. Finally, it is known that the multi-camera Tomo-PIV system can reconstruct higher density seeding particles than the single-camera LF-PIV technique (Scarano 2013; Fahringer et al. 2015; Shi et al. 2016, 2017). Although the same physical seeding density (particle/mm<sup>3</sup>) could be used when performing simulation studies between LF-PIV and Tomo-PIV, tests completed in this section are based on synthetic images that feature the most favourable seeding density of each technique. In such way, both LF-PIV and Tomo-PIV can fully demonstrate their potentials, consistent with each experiment being individually optimised for a given field of view.

Based on the above analysis, comparative studies in this section were performed for the two techniques by varying key parameters such as the number of Tomo-PIV cameras, PMR and LTPR. For such purposes, a series of synthetic light-field PIV images and Tomo-PIV images were generated using data from a direct numerical simulation of an incompressible jet (Fig. 2a). The Reynolds number of the DNS was 2500, corresponding to a circular nozzle diameter of  $D=40$  mm and a jet exit velocity of 0.13 (dimensionless). Synthetic PIV images were generated for a measurement volume located ( $x=0.5D$ ,  $y=0.5D$ ,  $z=1D$ ) from the nozzle exit (Fig. 2b). It should be noted that, to reduce the computational load without losing generality, relatively low-resolution synthetic Tomo-PIV cameras and light-field cameras are constructed in this section.

## 2.1 Generation of synthetic light-field particle images

To generate synthetic light-field particle images the two-plane parameterisation of the 4D plenoptic function is used in this study (Levoy and Hanrahan 1996). Figure 3 illustrates the basic ray tracing process for generating the synthetic images. Definition of the parameters in the figure are:  $S_o$  is the object distance;  $S_i$  is the image distance;  $f_m$  is the focal length of the main lens;  $f_l$  is the focal length of the micro-lens;  $p_m$  is the aperture of the main lens;  $p_l$  is the microlens pitch;  $p_p$  is the pixel pitch;  $S_y$  is the coordinate of lenslet centre. Linear optics was used to calculate the spatial location of each ray during its propagation from tracer particles to the image sensor. For example, for a tracer particle located at  $dy$  above the optical axis and  $dz$  away from the focal plane,

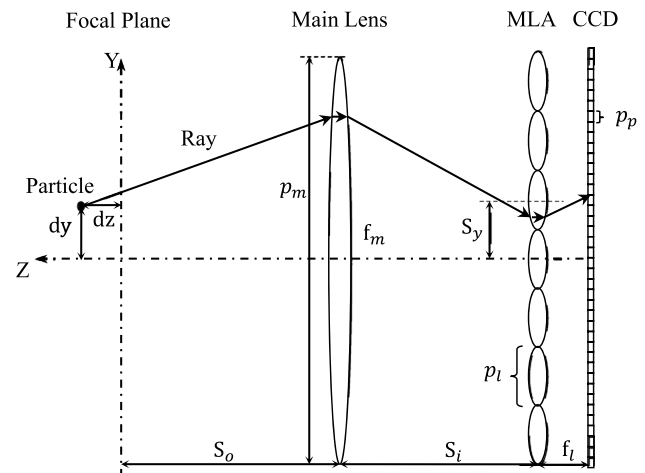


**Fig. 3** Schematic of synthetic light-field particle image generation (1D model)

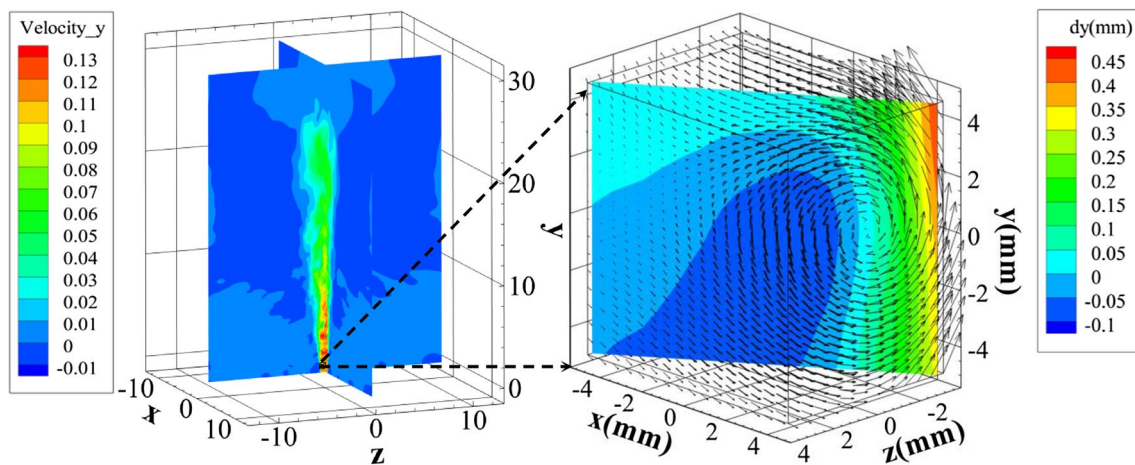


**Fig. 2** **a** Overview of the DNS jet flow field; **b** synthetic measurement volume

the propagation of its scattered rays can be traced from the main lens, through the MLA and finally to the image sensor using equations detailed in Georgiev and Intwala (2003) and Shi et al. (2016).

In this section, the synthetic light-field camera is arranged in a way that its sensor plane is parallel to the jet direction ( $x$ – $y$  plane in Fig. 2) and its optical axis is along the  $z$ -direction (see Fig. 2). To generate the first frame of the synthetic light-field particle image, a set of random particle coordinates are generated. From each particle, five million rays are simulated spanning the aperture of the main lens and the locations where these rays hit the image sensor are calculated according to equations detailed in Georgiev and Intwala (2003) and Shi et al. (2016). Pixel intensities of the synthetic light-field particle image are calculated based on the number of rays received by each pixel, and are normalised to the range of 0–255. After that, these random particles are shifted according to the DNS flow with a given time interval such that the maximum imaged particle displacement complies the one-quarter rule for the first pass of cross-correlation process. The ray tracing process is then repeated to generate the second frame of the light-field particle image.

To investigate the effects of PMR and LTPR on the performance of LF-PIV, two light-field camera sizes (e.g.  $800 \times 800$  pixel<sup>2</sup> and  $1600 \times 1600$  pixel<sup>2</sup>) with three different PMRs (e.g. PMR = 7, 14, 28) were simulated. Note that the hexagonal lenslet was simulated to achieve a better resolution (Shi et al. 2016). In addition, one Tomo-camera size (e.g.  $160 \times 160$  pixel) with three different configurations (e.g. Tomo-camera number  $N_c = 4, 6, 8$ ) were simulated, which results in six sets of LTPR cases (e.g. LTPR = 3.13, 4.17, 6.25, 12.5, 16.67 and 25). When constructing the artificial light-field cameras, the general principle of f-number matching between the main lens and microlens was applied to

maximise resolution (Ng et al. 2005). With a given pixel pitch, for example, the pixel size is set as 0.015 mm for the low LTPR case (see Table 1). When PMR varies, it changes the lenslet size and hence the focal length of the lenslet needs to be adjusted accordingly to maintain the same f-number as the main lens. To illustrate these relationships, schematics of relative geometric configurations of the different synthetic light-field cameras under consideration are shown in Fig. 4. For all synthetic light-field images, particle density is set to 0.5 particle per microlens (ppm) which was determined as the optimal density from our previous study (Shi et al. 2016). An example of a synthetic light-field particle image is shown in Fig. 5a–c. Detailed information on parameters used in synthetic particle image generation is listed in Table 1. Note that these parameters are purely for theoretical analysis, and the possibility of manufacturing such light-field cameras are not considered here.

## 2.2 Generation of synthetic tomographic particle images

Synthetic tomographic particle image is generated for an array of cameras equally spaced around the cubic reconstruction volume in the  $x$ – $z$  plane with camera numbers ranging from 4, 6 and 8 (Fig. 6). The projection of 3D tracer particles to 2D image plane is calculated using a pinhole camera model (Tsai 1986) with a focal length of 85 mm. The image distance and object distance are 93.4 and 946.5 mm, respectively, which result in a magnification factor of 0.075 mm/pixel. A set of random particles are generated in the measurement volume, and their projections in each camera sensor are calculated by the camera matrix, which gives the image coordinate of the particle image centre. Subsequently, a Gaussian distribution is applied to the calculated

**Table 1** Key parameters used for synthetic image generation (note that the low LTPR and high LTPR each corresponds to only one type of light-field camera resolution, e.g.  $800 \times 800$  and  $1600 \times 1600$ . The six sets of LTPR cases are simply a result of different Tomo-camera number)

LF-PIV							Tomo-PIV			
Camera number	1						$N_c = 4, 6, 8$			
LTPR	Low			High			–			
	6.25, 4.17, 3.13			25, 16.67, 12.5						
Pixel resolution of each camera	800×800			1600×1600			160×160			
Field of view	12×12×10 mm <sup>3</sup>									
$p_p$ (mm)	0.015			0.0075			0.075			
PMR	7	14	28	7	14	28	–			
MLA resolution	114×132	57×66	29×33	228×264	114×132	57×66	–			
$p_l$ (mm)	0.105	0.210	0.420	0.0525	0.105	0.210	–			
Particle density	ppm	0.5					–			–
	ppp	0.0118	0.0029	0.0007	0.0118	0.0029	0.0007	0.05	0.1	
Particle number	7524	1881	470	30,096	7524	1881	1280	2560		



**Fig. 4** Schematics of synthetic light-field camera configurations for: **a** PMR=7, LTPR=3.13, 4.17, 6.25; **b** PMR=14, LTPR=3.13, 4.17, 6.25; **c** PMR=28, LTPR=3.13, 4.17, 6.25; **d** PMR=7, LTPR=12.5, 16.67, 25; **e** PMR=14, LTPR=12.5, 16.67, 25; **f** PMR=28, LTPR=12.5, 16.67, 25 (Note that the separation between MLA and CCD varies due to the variation of MLA focal length, which is caused by different PMR)

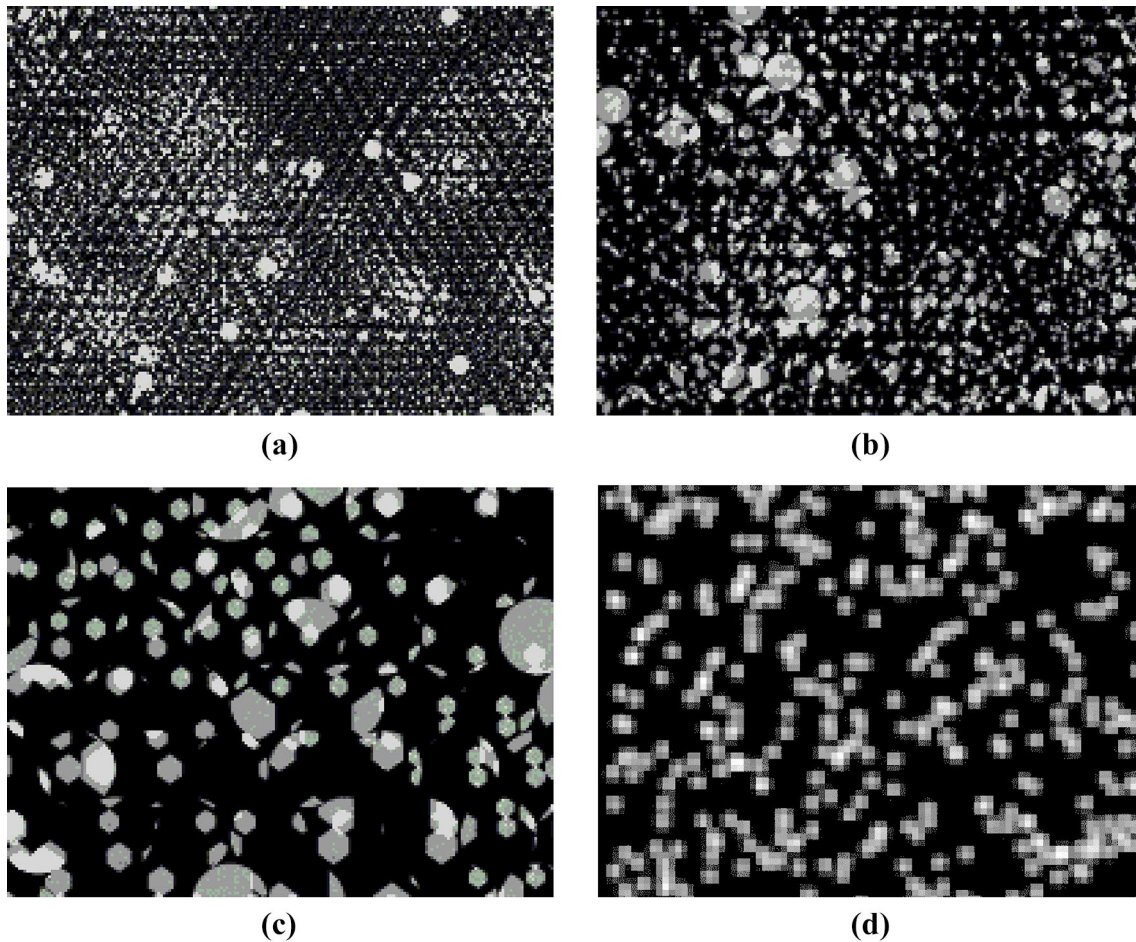
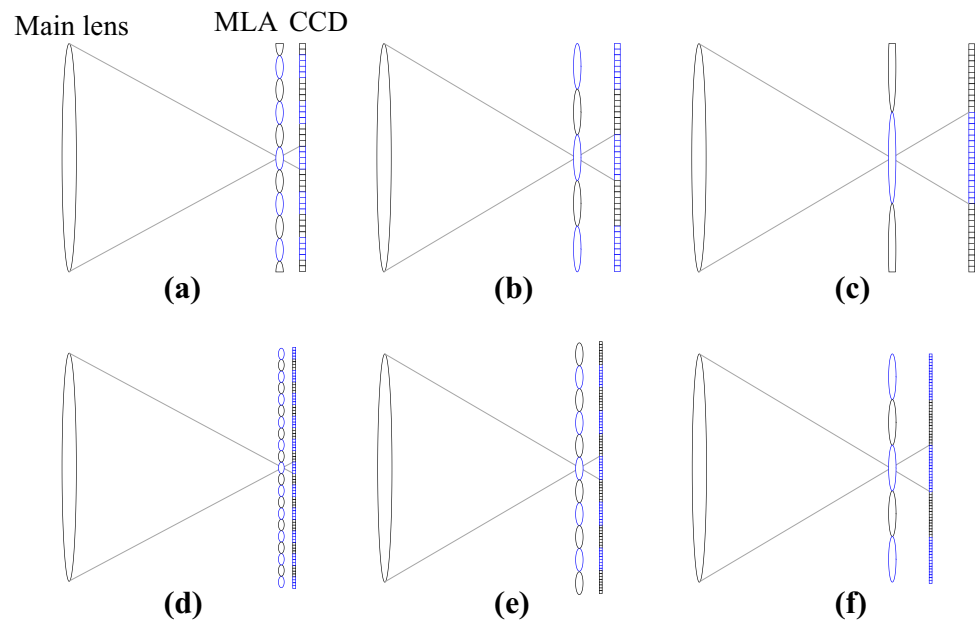


**Fig. 5** Example of synthetic particle images **a** LF-PIV (LTPR=3.13, 4.17, 6.25, PMR=7, 0.5 ppm); **b** LF-PIV (LTPR=3.13, 4.17, 6.25, PMR=14, 0.5 ppm); **c** LF-PIV (LTPR=3.13, 4.17, 6.25, PMR=28, 0.5 ppm); **d** Tomo-PIV (0.05 ppp)

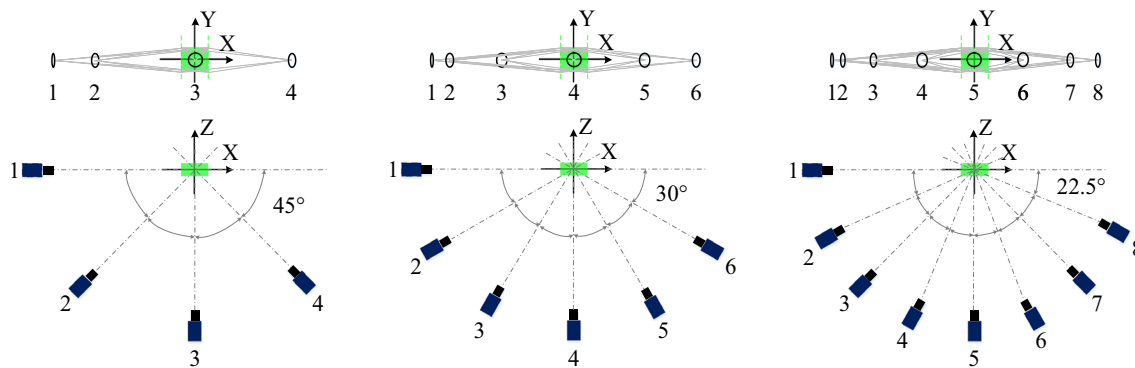


**Fig. 6** Camera configurations used for synthetic tomographic particle image generation

image coordinate to generate a particle image with a diameter around 3 pixels. Applying this process to each camera produces the first frame of synthetic tomographic particle images. To produce the second frame of the particle image set, the random particles are shifted to a distance calculated by the DNS flow with a given time interval so that the maximum particle image displacement corresponds to one quarter of the initial interrogation window size. These particles are then projected to each camera sensor in a similar fashion as generating the first frame of particle images. An example of synthetic tomographic particle image is shown in Fig. 5d.

### 2.3 Simulation results

To conduct the simulation tests, synthetic light-field and tomographic particle image pairs are first reconstructed by the DRT-MART (Shi et al. 2017) and MLOS-SMART (Atkinson and Soria 2009) algorithms, respectively. Instead of using 1:1 pixel voxel ratio, which is normally the case for Tomo-PIV, light-field particle image reconstruction employs a different pixel voxel ratio in  $x$ -,  $y$ - and  $z$ -directions. This is mainly due to the elongation effect of the reconstructed particles, especially in  $z$ -direction. Previous studies demonstrate that the pixel voxel ratio of 2:2:10 in  $x$ -,  $y$ - and  $z$ -direction achieves a good balance between reconstruction accuracy and computational cost (Shi et al. 2017). After particle image reconstruction, instantaneous velocity fields are then calculated with a two-pass, three-dimensional multi-grid cross-correlation method (Soria 1996), with an overlapping ratio of 0.75. While the first interrogation window size is chosen according to the one-quarter rule, the final interrogation window size is determined such that there are 7–10 particles on average in each window. Incorrect velocity vectors are detected by a  $3 \times 3 \times 3$  median filter (Westerweel and Scarano 2005), only valid vectors were considered in the subsequent analysis. Detailed information on the reconstruction and cross-correlation parameters used for different test cases is listed in Table 2 below. Considering the extensive

computational cost required by DRT-MART and MLOS-SMART reconstruction as well as three-dimensional cross-correlation, all calculations are accelerated by GPU parallel processing via a NVIDIA TITAN X GPU unit.

To reveal the influences of LTPR, PMR and particle density on the performance of LF-PIV and Tomo-PIV, accuracy of the reconstructed particle position is analysed for the two techniques. As the reconstructed particles are elongated in the  $z$ -direction for both techniques, the centre coordinates are calculated using the peak centroid method instead of Gaussian peak fitting. By comparing the reconstructed particle centre with its ground truth, the probability density function (PDF) of the reconstruction errors in  $x$ -,  $y$ - and  $z$ -directions is plotted in Fig. 7 for all tested cases.

Figure 7a, b presents the particle centre reconstruction errors for Tomo-PIV, which show that the reconstruction accuracy increases with an increase in camera number, but decreases with an increase in particle density. Such observations are in line with previous studies which demonstrated that more viewing angles and less seeding particles would help to mitigate the elongation effects, as well as reducing “ghost particles”, both of which contribute to a better reconstruction accuracy (Elsinga et al. 2006; Scarano 2013). On the other hand, the reconstruction accuracy of LF-PIV is strongly affected by the camera resolution (or LTPR). As shown in Fig. 7c, d, doubling the light-field camera pixel resolution would nearly double the particle centre reconstruction accuracy in both  $x$ - and  $y$ -directions. For the  $z$ -direction reconstruction accuracy, although it is primarily governed by the PMR, as already been proven that the depth resolution is highly dependent upon the number of pixels beneath each lenslet (Shi et al. 2016), it is also slightly affected by the LTPR. As shown in Fig. 7d, higher LTPR clearly degrades the reconstruction error with a larger magnitude (i.e. error  $> 0.004$  mm) for all current PMR cases. This is because that, for the same PMR, higher LTPR would effectively increase the MLA resolution (e.g. PMR = 7, Fig. 4a, d). With higher MLA

**Table 2** Reconstruction and interrogation parameters used for synthetic image processing

	LF-PIV						Tomo-PIV		
LTPR	Low			High			–		
	6.25, 4.17, 3.13			25, 16.67, 12.5					
PMR	7	14	28	7	14	28	ppp=0.05	ppp=0.1	
Reconstruction	DRT-MART						MLOS-SMART		
Iteration number	400						40		
Pixel voxel ratio	2:2:10						1:1:1		
Reconstruction volume (voxel)	400×400×67			800×800×134			160×160×133		
Voxel size (mm)	0.03×0.03×0.15			0.015×0.015×0.075			0.075×0.075×0.075		
First window (voxel)	x-	80	160	320	80	160	320	64	32
	y-	80	160	320	80	160	320	64	32
	z-	16	32	64	16	32	64	64	32
Second window (voxel)	x-	40	80	160	40	80	160	32	16
	y-	40	80	160	40	80	160	32	16
	z-	8	16	32	8	16	32	32	16
Second window (mm <sup>3</sup> )	1.2 <sup>3</sup>	2.4 <sup>3</sup>	4.8 <sup>3</sup>	0.6 <sup>3</sup>	1.2 <sup>3</sup>	2.4 <sup>3</sup>	2.4 <sup>3</sup>	1.2 <sup>3</sup>	

resolution, a small particle displacement in z-direction will result in light rays been captured by more lenslet and more pixels, which in return will help to better resolve the particle location during the reconstruction process. Details of which can be found in Shi et al. (2016) (especially refer to Fig. 9 in the reference). Cross comparing the results shown in Fig. 7a, c, it would suggest that LF-PIV is likely to achieve similar accuracy as Tomo-PIV at low LTPR, PMR28 test case.

To compare the performance of these two techniques further, the calculated instantaneous velocity vectors are compared with the original DNS velocity field, which is spatially filtered to match the final interrogation window size. The RMS errors for each velocity component are plotted in Fig. 8. Starting with the LF-PIV simulation results first (Fig. 8a), for the low-resolution light-field camera (LTPR = 3.13, 4.17, 6.25), the measurement error increases with PMR, although higher PMR offers better depth resolution (Shi et al. 2016). However, for a given number of pixels, an increasing in PMR can only be achieved by increasing the physical dimension of each lenslet, which effectively reduces the overall number of microlens (decreased MLA resolution). As a result, it leads to a reduction in the effective particle density, and hence limits the final interrogation window size (Table 1). For the higher resolution light-field camera (LTPR = 12.5, 16.67, 25), as the MLA resolution is nearly doubled (doubling the seeding density), the overall measurement error is greatly reduced for x-, y- and z-direction velocity components ( $u$ ,  $v$  and  $w$ , respectively). This is particularly true for the PMR = 14 case, which achieves the best balance between depth resolution (PMR) and particle density (MLA resolution), and produces the lowest RMS error for the w-velocity component (around 0.15 pixels).

Figure 8b shows the variation of RMS error with the number of cameras used in Tomo-PIV. In general, increasing the number of cameras from four to eight gradually improves the measurement accuracy as shown by (Elsinga et al. 2006; Atkinson and Soria 2009), especially for the  $v$ -velocity component. This is due to the improved reconstruction quality in the y-direction, which is parallel to the image planes of these cameras. However, possibly due to the increased ghost particles when particle density is too high, the measurement error for PPP = 0.1 case is slightly higher than the PPP = 0.05 case (Elsinga et al. 2006; Scarano 2013). Note that single-camera LF-PIV does not suffer from the ghost particle reconstruction problem according to our previous studies (Shi et al. 2017). Comparing the results between LF-PIV and Tomo-PIV, it is clear that the measurement accuracy of single-camera LF-PIV is comparable with the four-camera Tomo-PIV system at a relatively low-pixel resolution ratio (e.g. LTPR = 3.13, 4.17, 6.25, PMR = 7), which matches well with the observations made with Fig. 8a, c. LF-PIV can achieve accuracy equal to or higher than Tomo-PIV for the same field of view as the number of pixels continues to increase beyond that of Tomo-PIV and a greater number of microlenses are used (e.g. PMR = 14; LTPR ≥ 25, for four-camera Tomo-PIV; LTPR ≥ 16.67, for six-camera Tomo-PIV; LTPR ≥ 12.5, for eight-camera Tomo-PIV).

In addition to performance analysis, the computational times that the two techniques spent on particle reconstruction are compared based on current state-of-the-art hardware (NVIDIA TITAN X GPU). Note that the computational times are normalised by the reconstruction cost of the four-camera Tomo-PIV. In general, LF-PIV would take significantly longer computational time as compared to Tomo-PIV. This is due to the relationship between the

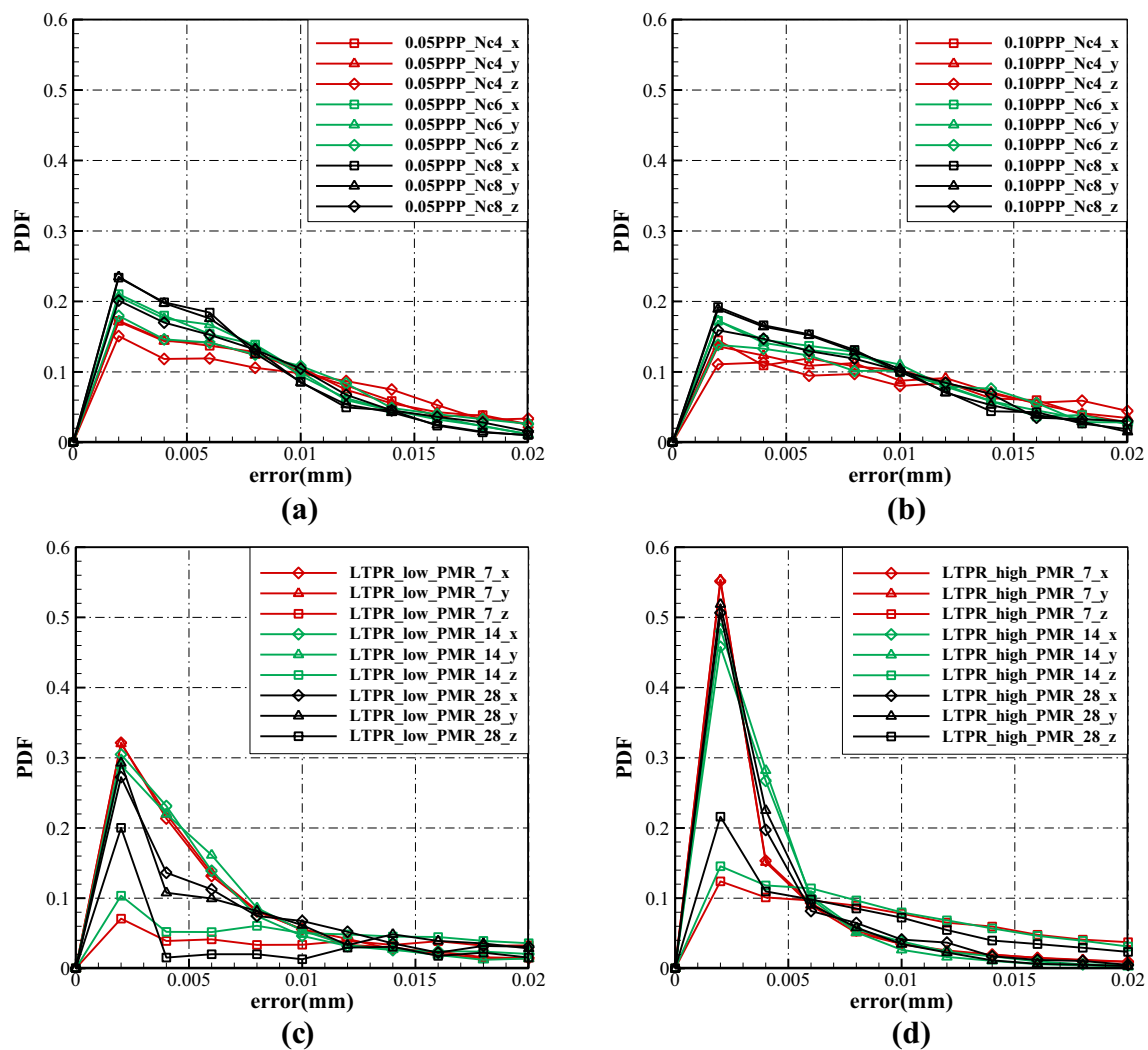


**Fig. 7** Particle centre reconstruction errors of the reconstructed particle position: **a** Tomo-PIV, 0.05PPP; **b** Tomo-PIV, 0.1ppp; **c** LF-PIV, low LTPR; **d** LF-PIV, high LTPR

voxel and the pixel in LF-PIV not based on a one-to-one mapping (which is the case in Tomo-PIV), and hence there are more non-zero pixels that need to be taken into consideration during the reconstruction stage in LF-PIV. Specifically, the reconstruction time of LF-PIV varies significantly with PMR and LTPR. Take for instance, the longest reconstruction time is incurred for  $\text{PMR} = 7$  case. As a matter of fact, a lower PMR means a smaller lenslet (Fig. 4), which effectively results in higher particle number for the same given ppm (Table 1; Fig. 5a–c). On the other hand, although the  $\text{PMR} = 28$  case has the lowest particle number for the same LTPR (Table 1), a non-zero voxel would affect almost all of the  $28 \times 28$  pixels beneath each affected lenslet. Therefore, the total number of pixels involved in reconstruction calculation is actually larger than that of  $\text{PMR} = 14$  (Table 3).

### 3 Experimental tests

Simulation studies in Sect. 2 demonstrate the key parameters that influence the relative performance of LF-PIV and Tomo-PIV; however, do not take into account the effects of background noise, lens distortion, misalignment between tomographic cameras as well as misalignment between MLA and image sensor in a light-field camera. To conduct a direct comparison, the LF-PIV and Tomo-PIV experimental systems are used to perform simultaneous measurements on the same volume of a low-speed jet flow. A schematic of the experimental setup is presented in Fig. 9, which shows that the sensor plane of the LF-PIV is parallel to the jet direction and the four tomographic cameras are positioned in a cross-like configuration.



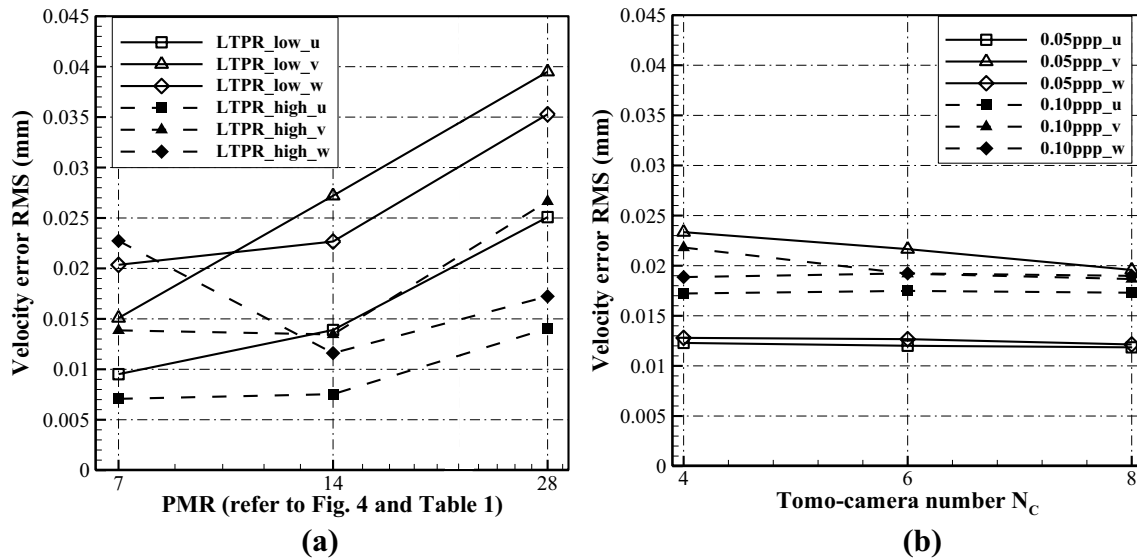


**Fig. 8** Simulation results for **a** LF-PIV for the low (LTPR = 3.13, 4.17, 6.25) and high-resolution (LTPR = 12.5, 16.67, 25) light-field cameras **b** Tomo-PIV (pixel size = 0.075 mm)

**Table 3** LF-PIV and Tomo-PIV reconstruction times for different PMR and particle density

	Reconstruction time				
	LF-PIV		Tomo-PIV		
	LTPR = 6.25, 4.17, 3.13	LTPR = 25, 16.67, 12.5		Particle density = 0.05 PPP	Particle density = 0.10 PPP
PMR = 7	55.9811	1269.4	$N_c = 4$	1	1.0093
PMR = 14	3.7750	15.2940	$N_c = 6$	1.1405	1.1550
PMR = 28	7.2170	55.2826	$N_c = 8$	1.3690	1.3744

**Table 4** Reconstruction and interrogation parameters used for experimental image processing

	LF-PIV	Tomo-PIV
Camera number	1	4
Effective resolution of each camera	6600 × 4400	480 × 320
Field of view (mm <sup>3</sup> )	38 × 26 × 10	
$p_p$	0.0058 mm/pixel	0.079 mm/pixel
Particle density	0.06 ppm	0.062ppp
MLA resolution	450 × 350	—
LTPR	47.27	—
PMR	14	—
Pixel voxel ratio	2:2:10	1:1:1
Reconstruction resolution (voxel)	3300 × 2200 × 182	480 × 320 × 130
Voxel size (mm)	0.012 × 0.012 × 0.055	0.079 × 0.079 × 0.079
First interrogation window size (voxel)	320 × 320 × 64	64 × 64 × 64
Second interrogation window size (voxel)	160 × 160 × 32	32 × 32 × 32
Spatial resolution (mm <sup>3</sup> )	1.84 × 1.84 × 1.76	2.53 × 2.53 × 2.53
Vector number	79 × 51 × 19	57 × 37 × 13

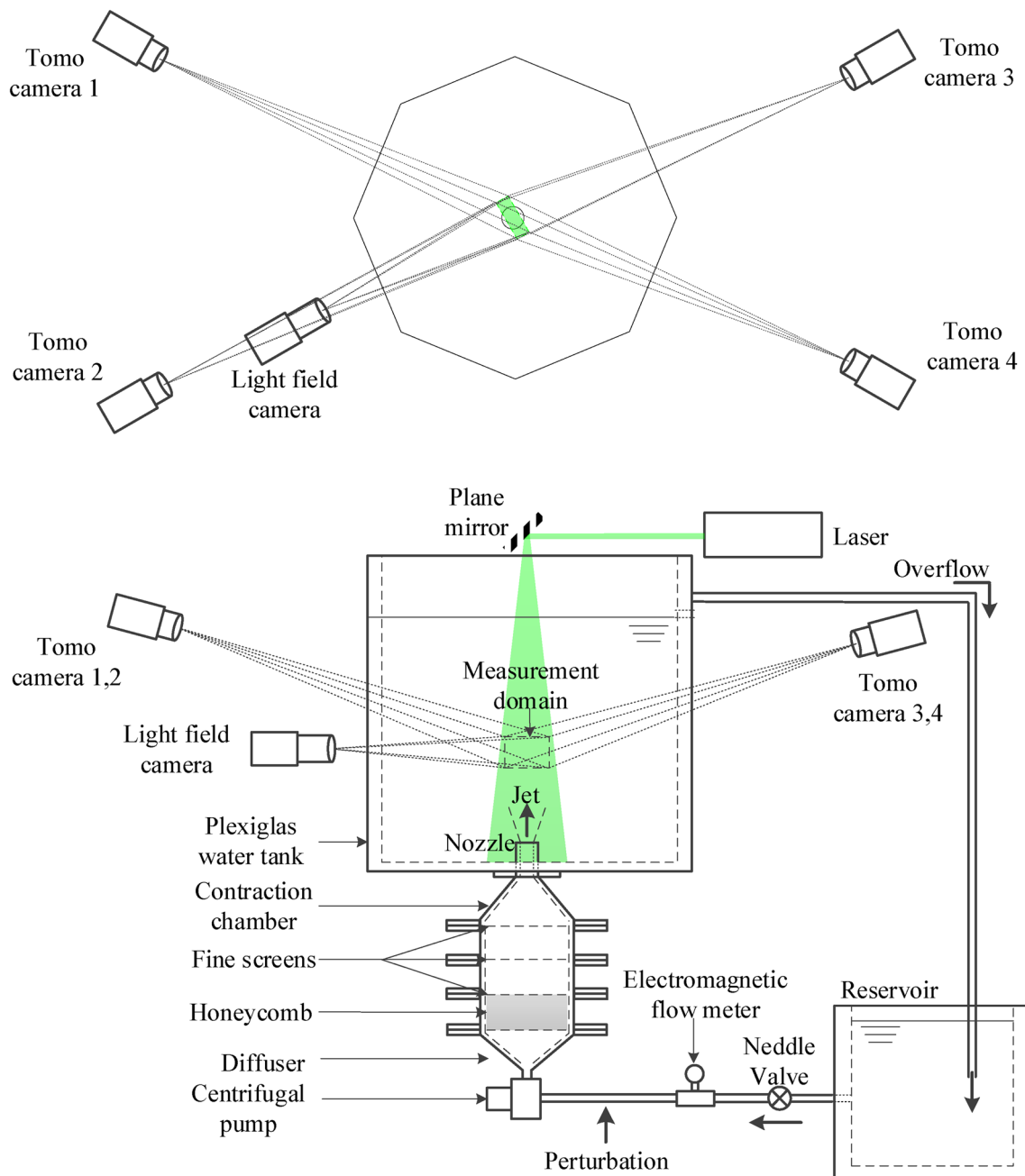
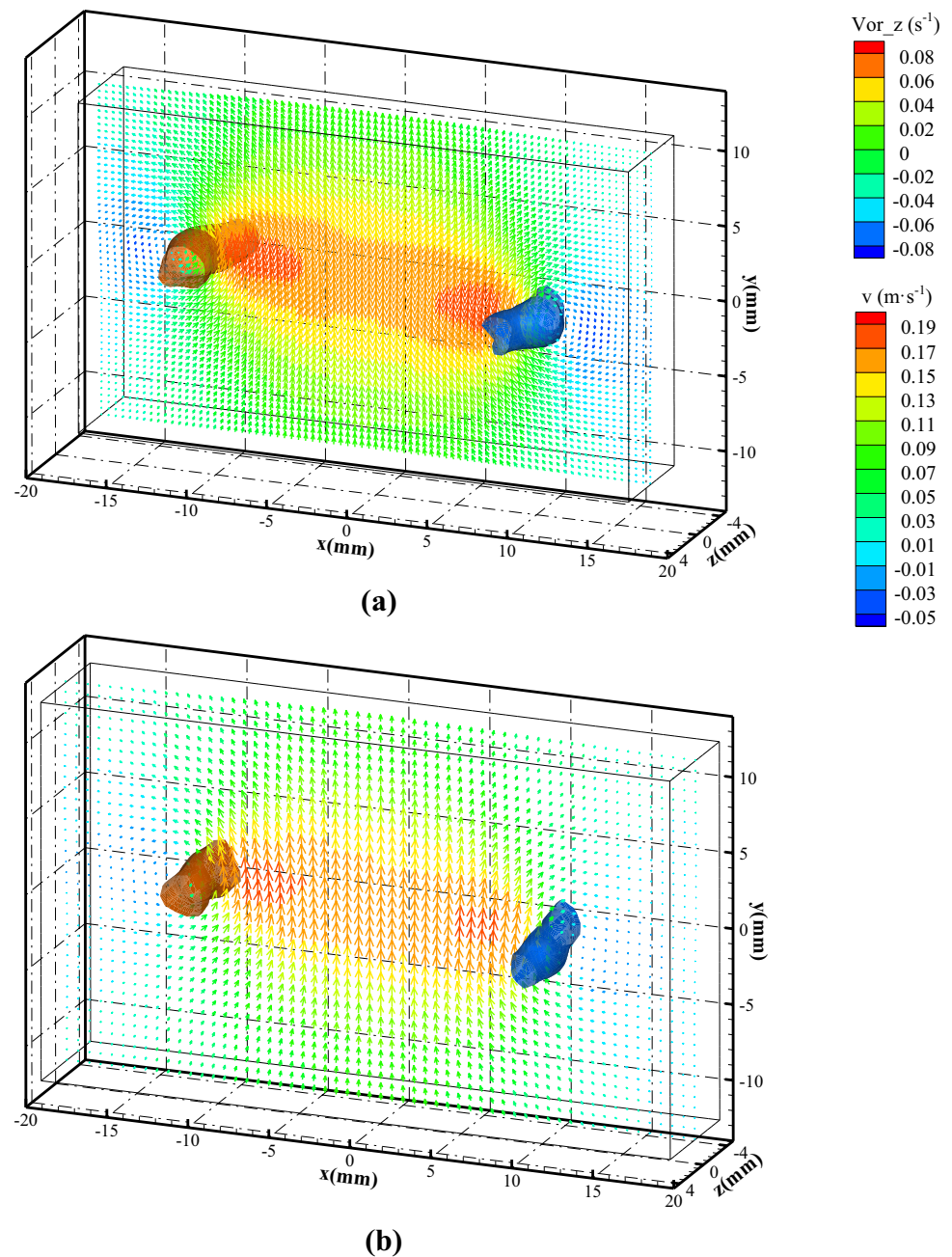


**Fig. 9** Schematics of the low-speed jet flow experimental setup

The flow scenario was produced by a recirculating pump and a  $D=20$  mm circular nozzle. Reynolds number tested was  $Re_D=2000$  and the measurement volume was approximately  $1.9 D \times 1.3 D \times 0.5 D$  along the  $x$ -,  $y$ -,  $z$ -directions and located at about  $2.25 D$  above the nozzle exit. Tracer particles were uniformly seeded in the water tank (Dantec dynamics  $20 \mu\text{m}$ ,  $\rho = 1.03 \text{ g/cm}^3$  polyamide seeding particles), which resulted in a seeding density of  $0.062 \text{ ppp}$  for

Tomo-PIV and  $0.06 \text{ ppm}$  for LF-PIV. Note that such density is optimal for Tomo-PIV and slightly sparse for LF-PIV. Illumination was provided by a 10-mm-thick laser sheet (Beamtech double pulse Nd: YAG laser,  $200 \text{ mJ/pulse}$ ,  $532 \text{ nm}$ ). Readers are referred to Shi et al. (2017) for more details on the experiment setup. Light-field particle images were captured by an in-house light-field camera (equipped with a Micro-NIKKOR  $200 \text{ mm}$  lens), which was developed

**Fig. 10** Phase-averaged jet flow field measured by **a** LF-PIV and **b** Tomo-PIV



from a 29M pixel Imperx B6640 PIV camera (Shi et al. 2016). Tomographic particle images were captured by four 4M pixel Imperx B2014 PIV cameras (each equipped with a Micro-NIKKOR 85 mm Scheimpflug lens). The five cameras were synchronised via a pulse generator and connected to the host computer (Dell Precision T7910) via four EPIX PIXCI E4 frame grabbers. To measure the phase-averaged flow field, a 1 Hz perturbation was introduced into the flow delivery pipe before the settling chamber, where it was synchronised with the five cameras and the laser pulse.

To facilitate the comparison of these two techniques, 20 instantaneous light-field and tomographic particle image

pairs were captured. The effective resolution of light-field camera and tomographic cameras used in this experiment are  $6600 \times 4400 \text{ pixel}^2$  and  $480 \times 320 \text{ pixel}^2$ , respectively, which results in a LTPR of 47.27. The light-field particle images were reconstructed with the DRT-MART method (400 iterations), and the tomographic particle images were sequentially processed with the self-volume calibration (Wieneke 2008) and 40-iteration MLOS-SMART method (Atkinson and Soria 2009). For light-field particle image reconstruction, the pixel voxel ratio was set as 2:2:10 in  $x$ -,  $y$ - and  $z$ -direction, which results in a reconstruction domain of  $3300 \times 2200 \times 182$  voxels. For Tomo-PIV reconstruction, the

pixel voxel ratio is maintained at 1:1 for all directions, which results in a reconstruction domain of  $480 \times 320 \times 130$  voxels. It should be noted that, although a light-field camera with a high pixel resolution produces a high-resolution reconstruction in the image plane, owing to limited angular resolution of single light-field camera, such high pixel resolution does not result in a higher depth resolution ( $z$ -direction in this case) than the Tomo-PIV. After particle intensity field reconstruction, instantaneous velocity fields were calculated with a three-dimensional multi-grid cross-correlation algorithm with 75% overlap. Initial and final interrogation windows are  $320 \times 320 \times 64$  voxels,  $160 \times 160 \times 32$  voxels for LF-PIV, and  $64 \times 64 \times 64$  voxel,  $32 \times 32 \times 32$  voxel for Tomo-PIV. Despite the difference in reconstruction resolution, the non-dimensionalised final interrogation window size for LF-PIV and Tomo-PIV is  $0.092D \times 0.095D \times 0.088D$  and  $0.13D \times 0.13D \times 0.12D$ , respectively. To summarise, key experimental parameters are listed in Table 4.

Any spurious vectors, which were 4.1% for LF-PIV and 5.2% for Tomo-PIV, were conservatively validated by  $3 \times 3 \times 3$  median filter and replaced with linear interpolation. Reconstruction and cross-correlation process were both accelerated by a NVIDIA TITAN X GPU unit, which took 4.5 h for LF-PIV reconstruction, and 10.7 s for Tomo-PIV reconstruction. The phase-averaged jet flow fields as measured by LF-PIV and Tomo-PIV are presented in Fig. 10, which shows the vorticity contour together with velocity vectors (colours represent the velocity component in the jet direction). Both LF-PIV and Tomo-PIV are shown to successfully capture the vortex roll-up along the jet shear layer, with the overall flow structure looking similar between the two techniques. By performing a cross-correlation between these two flow fields, the correlation coefficient was 0.94, indicating a high level of agreement between the LF-PIV and Tomo-PIV results.

## 4 Conclusions

A direct comparison between the single-camera light-field particle image velocimetry (LF-PIV) and multi-camera tomographic particle image velocimetry (Tomo-PIV) was carried out in the current study. Comparisons were performed using both synthetic light-field and tomographic particle images as well as experimental images of a round jet flow. Results demonstrate that the single-camera LF-PIV can achieve accuracy equivalent to or better than that of the multi-camera Tomo-PIV for the same field of view, but doing so requires a relatively high PMR and LTPR. Meanwhile, for the same total number of pixels, single-camera LF-PIV cannot match the seeding density or spatial resolution of Tomo-PIV due to its smaller angular resolution. The present comparative study between the novel

single-camera LF-PIV and traditional multi-camera Tomo-PIV points out the significant potential of such single-camera-based volumetric velocity measurement technique, owing to its greater simplicity of the experimental setup and the ability to provide accurate 3C-3D flow measurements even in applications where optical access is limited.

**Acknowledgements** Financial support provided by National Natural Science Foundation of China (Grant no. 11472175), Shanghai Raising Star Program (Grant no. 15QA1402400) and Singapore Ministry of Education AcRF Tier-2 Grant (Grant no. MOE2014-T2-1-002) is gratefully acknowledged. The support of Australian Research Council (ARC) for this work is gratefully acknowledged; Dr. Atkinson was supported by an ARC Discovery Early Career Researcher Award (DECRA) fellowship while undertaking this work.

## References

- Adrian RJ (1984) Scattering particle characteristics and their effect on pulsed laser measurements of fluid flow: speckle velocimetry vs. particle image velocimetry. *Appl Opt* 23:1690–1691
- Adrian R, Westerweel J (2011) Particle image velocimetry. Cambridge University Press, Cambridge
- Atkinson C, Soria J (2009) An efficient simultaneous reconstruction technique for tomographic particle image velocimetry. *Exp Fluid* 47:553–568
- Belden J, Truscott T, Axiak M, Techet A (2010) Three-dimensional synthetic aperture particle image velocimetry. *Meas Sci Technol* 21:1–21
- Ding J, Wang J, Liu Y, Shi S (2015) Dense ray tracing based reconstruction algorithm for light-field volumetric particle image velocimetry. In: 7th Australian Conference on Laser Diagnostics in Fluid Mechanics and Combustion. Melbourne, Australia
- Elsinga G, Scarano F, Wieneke B, van Oudheusden B (2006) Tomographic particle image velocimetry. *Exp Fluid* 41:933–947
- Fahringer T, Lynch K, Thurow B (2015) Volumetric particle image velocimetry with a single plenoptic camera. *Meas Sci Technol* 26:115201
- Georgiev T, Intwala C (2003) Light-field camera design for integral view photography. Adobe Tech Report
- Georgiev T, Zheng K, Curless B, Salesin D, Nayar S, Intwala C (2006) Spatio-angular resolution trade off in integral photography. In: Eurographics Symposium on Rendering
- Hinsch K (2002) Holographic particle image velocimetry. *Meas Sci Technol* 13:R61–R72
- Levoy M, Hanrahan P (1996) Light field rendering. *ACM Trans Graph* 31–42
- Li H, Ding J, Zhao Z, Qu W, Xiong J, Shi S (2017) Investigation of 3D flow behaviour inside a  $3 \times 3$  rod bundle using Light Field-PIV and the matched refractive index techniques. In: The 12th International Symposium on Particle Image Velocimetry. Busan, Korea
- Lumsdaine A, Georgiev T (2009) The focused plenoptic camera. In: Computational Photography (ICCP), 2009 IEEE International Conference on
- Meng H, Pan G, Pu Y, Woodward S (2004) Holographic particle image velocimetry from film to digital recording. *Meas Sci Technol* 15:673–685
- Ng R, Levoy M, Bredif M, Duval G, Horowitz M, Hanrahan P (2005) Light Field Photography with a Hand-Held Plenoptic Camera, tech. report CTSR 2005-02, Stanford University
- Palafox P, Oldfield M, LaGraff J, Jones T (2008) PIV maps of tip leakage and secondary flow fields on a low-speed turbine blade cascade with moving end wall. *J Turbomach* 130:011001



- Pereira F, Gharib M, Dabiri D, Modarress M (2000) Defocusing PIV: a three-component 3-D PIV measurement technique application to bubbly flows. *Exp Fluid* 29:S78–S84
- Scarano F (2013) Tomographic PIV: principles and practice. *Meas Sci Technol* 26:1–28
- Schanz D, Gesemann S, Schröder A (2016) Shake-the-box: Lagrangian particle tracking at high particle image densities. *Exp Fluid* 57:70
- Shi S, Wang J, Ding J, Zhao Z, New TH (2016) Parametric study on light-field volumetric particle image velocimetry. *Flow Meas Instrum* 49:70–88
- Shi S, Ding J, New TH, Soria J (2017) Light-field camera-based 3D volumetric particle image velocimetry with dense ray tracing reconstruction technique. *Exp Fluids* 58:78
- Soria J (1996) An investigation of the near wake of a circular cylinder using a video-based digital cross-correlation particle image velocimetry technique. *Exp Therm Fluid Sci* 12(2):221–233
- Tsai RY (1986) An efficient and accurate camera calibration technique for 3D machine vision. In: *Proceedings of IEEE conference on computer vision and pattern recognition*, Miami Beach, FL, USA, pp 364–374
- Wernet M, Van Zante D, Strazisar T, John W, Prahst P (2005) Characterization of the tip clearance flow in an axial compressor using 3-D digital PIV. *Exp Fluid* 39:743–753
- Westerweel J, Scarano F (2005) Universal outlier detection for PIV data. *Exp Fluid* 39:1096–1100
- Wieneke B (2008) Volume self-calibration for 3D particle image velocimetry. *Exp Fluid* 45:549–556
- Xu S, Ding J, Zhao Z, Atkinson C, Soria J, Shi S (2017) 3D flow measurements of circular air jet at  $Re = 30,000$  using light field particle image velocimetry. *The 12th International Symposium on Particle Image Velocimetry*. Busan, Korea